Progress In Electromagnetics Research, Vol. 119, 1–18, 2011

BISTATIC IMAGE FORMATION FROM SHOOTING AND BOUNCING RAYS SIMULATED CURRENT DISTRIBUTIONS

H. Buddendick and T. F. Eibert*

Technische Universität München, Lehrstuhl für Hochfrequenztechnik, Munich 80290, Germany

Abstract—Inverse Synthetic Aperture Radar (ISAR) imaging is one of the most sophisticated methods to obtain information about the scattering or radiation properties of a finite sized object. The idea is to process the scattered or radiated fields coherently over a certain frequency bandwidth and over a certain angular range in order to generate the image. In a simulation based approach, this procedure can be considerably simplified, if the source currents are known (either real or equivalent) and if a bistatic image is desired. By inserting the radiation integral into the imaging integral and by interchanging the integration orders, the imaging point spread function can be generated and the image formation is reduced to a convolution of the point spread function with the current distribution. A concise formulation of this well-known methodology is presented together with a discussion of important properties. Various examples of 2D and 3D images for complex metallic objects such as automobiles are shown, which have been obtained from the surface currents of a Shooting and Bouncing Rays (SBR) field solver.

1. INTRODUCTION

Inverse Synthetic Aperture Radar (ISAR) imaging is an established method for generating high-resolution images of scattering objects [1]. It is based on the coherent processing of radar signals, which are acquired for varying observation angles and for a certain band of frequencies. In an experimental approach, it is clear that ISAR must work with the waves scattered from the observed object. However, in

Received 2 June 2011, Accepted 30 June 2011, Scheduled 14 July 2011

* Corresponding author: Thomas F. Eibert (eibert@tum.de).

simulation based approaches there is no need to compute the scattered waves explicitly, as, e.g., done in [2]. It is rather possible to directly generate the ISAR image with the induced currents on the objects, which are usually available in an electromagnetic simulation such as integral equation solutions by the Method of Moments (MoM) [3, 4] or an Physical Optics (PO) based Shooting and Bouncing Rays (SBR) approach [5, 6]. First, such techniques were utilized for the generation of 1D (time-domain) downrange profiles [7, 8]. Later, the often ray-tube integration called approach was employed for 2D ISAR image generation [8] and it was even recognized that the resulting convolution integrals can be efficiently evaluated by Fast Fourier Transform (FFT) based fast convolutions [9]. In [10], the approach was extended to 3D image generation. The direct image generation methods are extremely fast and allow for an efficient extraction of the dominant scattering centers of an object, which can be used for compressed scattering center representations of the scattering behaviour of complex objects in the far-field [11] as well as in the near-field [12]. In [13], the technique was also studied for 2D imaging and later extended for a more general coordinate representation in [14]. Further applications of the direct imaging techniques are found in [15–17]. In contrast, many simulations in the radar imaging field are performed with the two-step approach of scattered field computation and subsequent image formation by SAR or ISAR processors [18, 19]. This is in particular the case if the SAR or ISAR processor shall be tested by simulated data or if secondary effects such as motion compensation must be considered.

In this paper, a concise vectorial representation of the formulation is given for the case of 3D ISAR imaging, which is also specialized to the 2D case. The pertinent small angle/small bandwidth point spread functions are given analytically for the 3D case together with all the first order correction terms usually not found in the literature. Important properties of the direct imaging approach are discussed and illustrated, in particular related to the required interpolations within the FFT accelerated convolutions. The images of complex objects are investigated, where the focus is on scattering center visualizations of automotive vehicles.

2. FORMULATION

2.1. Image Formation for Radiating Sources

Consider the radiated electric far-field $\mathbf{E}$ of an electric current distribution $\mathbf{J}$ confined to the source volume V according to [20]

$$\mathbf{E}(\mathbf{r},k) = -jkZ\frac{\mathrm{e}^{-jkr}}{4\pi r}\underbrace{\left(\bar{\mathbf{I}}-\hat{r}\hat{r}\right)}_{\left(\hat{\vartheta}\hat{\vartheta}+\hat{\varphi}\hat{\varphi}\right)}\cdot\iiint\limits_{V}\mathbf{J}(\mathbf{r}')\,\mathrm{e}^{jk\hat{r}\cdot\mathbf{r}'}\,d^3\mathbf{r}', \tag{1}$$

where a time factor $\mathrm{e}^{j\omega t}$ is assumed and suppressed. $k=\omega\sqrt{\varepsilon\mu}$ is the wavenumber and $Z=\sqrt{\mu/\varepsilon}$ is the characteristic impedance of the considered homogeneous medium (typically free space), respectively. $\hat{r}$ is the unit vector in direction of $\mathbf{r}$.
Introducing the spectral image representation

$$\tilde{\mathbf{J}}(\mathbf{k}) = \frac{-1}{jkZ}\frac{4\pi r}{\mathrm{e}^{-jkr}}\,\mathbf{E}(r\hat{r},k) \tag{2}$$

with $\mathbf{k}=k\hat{r}$ the ISAR imaging integral over the k-space observation domain $\mathcal{K}$ can be written as

$$\hat{\mathbf{J}}(\mathbf{r}) = \frac{1}{(2\pi)^3}\iiint\limits_{\mathcal{K}}\tilde{\mathbf{J}}(\mathbf{k})\,\mathrm{e}^{-j\mathbf{k}\cdot\mathbf{r}}\,d^3\mathbf{k} \tag{3}$$

and the spatial distribution of $\hat{\mathbf{J}}$ is interpreted as the image. Here it should be pointed out that $\hat{\mathbf{J}}$ may not contain gradient like non-radiating sources possibly contained in $\mathbf{J}$, as, e.g., discussed in [21].

Substituting (2) under consideration of (1) into (3) results in

$$\hat{\mathbf{J}}(\mathbf{r}) = \frac{1}{(2\pi)^3}\iiint\limits_{\mathcal{K}}\iiint\limits_{V}\left(\hat{\vartheta}\hat{\vartheta}+\hat{\varphi}\hat{\varphi}\right)\cdot\mathbf{J}(\mathbf{r}')\,\mathrm{e}^{-j\mathbf{k}\cdot(\mathbf{r}-\mathbf{r}')}\,d^3\mathbf{r}'\,d^3\mathbf{k}\,. \tag{4}$$

Changing the order of integrations gives

$$\hat{\mathbf{J}}(\mathbf{r}) = \iiint\limits_{V}\bar{\mathbf{P}}\left(\mathbf{r}-\mathbf{r}'\right)\cdot\mathbf{J}\left(\mathbf{r}'\right)\,d^3\mathbf{r}' \;=\; \bar{\mathbf{P}}(\mathbf{r})*\mathbf{J}(\mathbf{r}), \tag{5}$$

where the $*$ denotes convolution and $\bar{\mathbf{P}}(\mathbf{r})$ is the dyadic point spread function defined as

$$\bar{\mathbf{P}}(\mathbf{r}) = \frac{1}{(2\pi)^3}\iiint\limits_{\mathcal{K}}\left(\hat{\vartheta}\hat{\vartheta}+\hat{\varphi}\hat{\varphi}\right)\mathrm{e}^{-j\mathbf{k}\cdot\mathbf{r}}\,d^3\mathbf{k}\,. \tag{6}$$

In Cartesian vector components, $\left(\hat{\vartheta}\hat{\vartheta}+\hat{\varphi}\hat{\varphi}\right)$ is

$$\begin{pmatrix} 1-\sin^2\vartheta\cos^2\varphi & -\sin\varphi\cos\varphi\sin^2\vartheta & -\sin\vartheta\cos\vartheta\cos\varphi \\ -\sin\varphi\cos\varphi\sin^2\vartheta & 1-\sin^2\vartheta\sin^2\varphi & -\sin\vartheta\cos\vartheta\sin\varphi \\ -\sin\vartheta\cos\vartheta\cos\varphi & -\sin\vartheta\cos\vartheta\sin\varphi & \sin^2\vartheta \end{pmatrix}, \tag{7}$$

where ϑ, φ are the spherical angles defining the observation direction corresponding to the direction of $\mathbf{k}$. Equation (5) provides for the possibility to directly compute an image as seen by an observer without the need to explicitly generate the observation fields. The imaging parameters such as observation bandwidth and observation aspect range are contained in the point spread function (6).

2.2. Image Formation for Scattering Problems

In the case of a scattering problem, the electric currents in (1) are induced by an incident field and are thus dependent on this field. An incident plane wave with propagation vector $\mathbf{k}_i$ is assumed to cause equivalent scattering currents

$$\mathbf{J}^s(\mathbf{r}') = \mathbf{J}(\mathbf{r}')\mathrm{e}^{-j\mathbf{k}_i\cdot\mathbf{r}'}\,, \tag{8}$$

where $\mathbf{J}(\mathbf{r}')$ now represents the spatial variations of these currents except for the extracted phase variations of the incident wave. In the spectral domain image representation of (2), $\mathbf{k}$ is now no longer equal to $\mathbf{k}_s = k\hat{r}$, it is rather identified as

$$\mathbf{k} = \underbrace{k\hat{r}}_{\mathbf{k}_s} - \mathbf{k}_i\,. \tag{9}$$

Under the assumption of a bistatic imaging configuration with one fixed $\mathbf{k}_i$, the above derivations and in particular (5) are still valid. However, in the monostatic case $\mathbf{J}(\mathbf{r}')$ may still depend on $\mathbf{k}_i$ and interchanging the integration orders in (4) will not be possible. Moreover, it should be noted that $\mathbf{J}(\mathbf{r}')$ may contain further phase variations due to particular scattering phenomena such as multiple interactions or material influences. If this is the case, the integration orders in (4) cannot be interchanged. However, in Section 2.4 it will be shown how multiple interaction effects can explicitly be considered. Further frequency and angle dependent terms such as reflection coefficients at material interfaces could also be extracted from $\mathbf{J}(\mathbf{r}')$ and considered within the point spread function. In the following, it is assumed that the change of integration orders is possible and focus will be on bistatic imaging.

2.3. Point Spread Functions Under Small Angle and Narrow Bandwidth Approximations

In order to facilitate a deterministic evaluation of the point spread function in (6), a small angle and narrow bandwidth approximation around $\varphi \approx 0, \vartheta' = \pi/2 - \vartheta \approx 0$ and $k \approx k_0$, respectively, is adopted

in the following. In view of the 2D-illustrations of the monostatic and bistatic k-space configurations in Fig. 1, the approximations

$$k_x \approx 2k, \tag{10}$$

$$k_y \approx 2c_g k_0 \varphi, \tag{11}$$

$$k_z \approx 2c_g k_0 \vartheta', \tag{12}$$

$$d^3\mathbf{k} \approx 8c_g^2 k_0^2 \, d\vartheta' d\varphi' dk \tag{13}$$

can be derived, where the factor c_g accounts for the fact that the origin of the spherical coordinate system representation of $\mathcal{K}$ is located at $(k_x, k_y, k_z) = (0, 0, 0)$ and $(k_x, k_y, k_z) = (k_0, 0, 0)$ for the monostatic and bistatic configurations, respectively. Consequently, $c_g = 1$ in the monostatic case and $c_g = 1/2$ in the bistatic case. The expression in (7) can also be simplified into

$$\begin{pmatrix} 0 & -\varphi & -\vartheta' \\ -\varphi & 1-\varphi^2 & -\vartheta'\varphi \\ -\vartheta' & -\vartheta'\varphi & 1 \end{pmatrix} \approx \begin{pmatrix} 0 & -\varphi & -\vartheta' \\ -\varphi & 1 & 0 \\ -\vartheta' & 0 & 1 \end{pmatrix}. \tag{14}$$

The evaluation of the k-space integrals in the representation of the point spread function (6) results then into

$$P_{yy}(\mathbf{r}) = P_{zz}(\mathbf{r}) = \frac{k_0^2}{8\pi^3} h\left(\Delta k, \frac{2x}{k_0}\right) h(\Delta\varphi, y) h(\Delta\vartheta, z) \mathrm{e}^{-j2k_0 x}, \tag{15}$$

$$P_{xy}(\mathbf{r}) = P_{yx}(\mathbf{r}) = \frac{k_0^2}{8\pi^3} h\left(\Delta k, \frac{2x}{k_0}\right) g(\Delta\varphi, y) h(\Delta\vartheta, z) \mathrm{e}^{-j2k_0 x}, \tag{16}$$

$$P_{xz}(\mathbf{r}) = P_{zx}(\mathbf{r}) = \frac{k_0^2}{8\pi^3} h\left(\Delta k, \frac{2x}{k_0}\right) h(\Delta\varphi, y) g(\Delta\vartheta, z) \mathrm{e}^{-j2k_0 x}, \tag{17}$$

where a bistatic configuration symmetric around the incident x-direction has been assumed and the quantities $\Delta k, \Delta\vartheta, \Delta\varphi$ define the extent of $\mathcal{K}$ as shown in Fig. 1. The 1D point spread functions $h(T, t)$ and $g(T, t)$ are

$$h(T, t) = T \, \mathrm{si}\left(\frac{T}{2} k_0 \, t\right), \tag{18}$$

$$g(T, t) = -jT \frac{\mathrm{si}\left(\frac{T}{2} k_0 \, t\right) - \cos\left(\frac{T}{2} k_0 \, t\right)}{t}. \tag{19}$$

The off-diagonal terms vanish along the x-axis and cause higher-order corrections with increasing distance to the x-axis.

The given point spread functions have been derived for rectangular windows in frequency and aspect angle. The consideration of other window functions is straightforward.

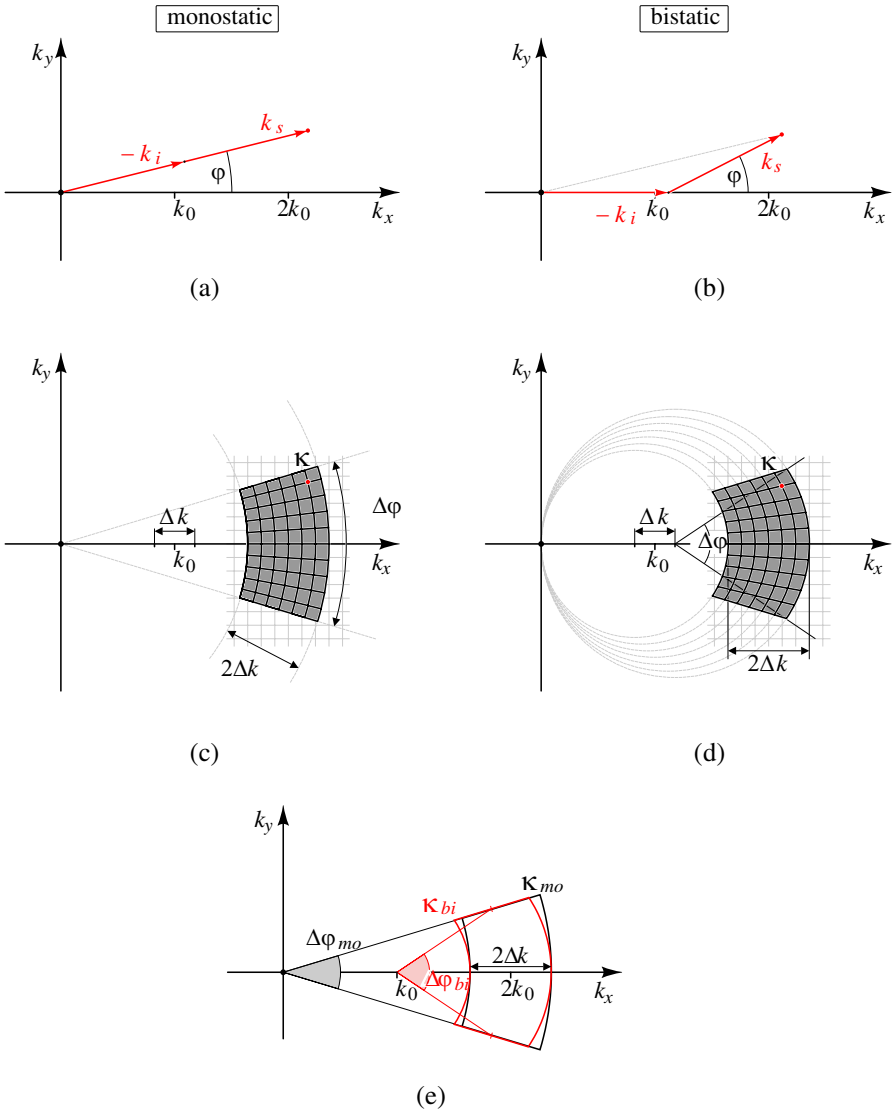

Figure 1. 2D k-space illustration according to (9): (a) monostatic k-vector, (b) bistatic k-vector, (c) monostatic integration domain $\mathcal{K}_{mo}$, (d) bistatic integration domain $\mathcal{K}_{bi}$ symmetric around the incident direction, (e) direct comparison of monostatic and bistatic integration domains.

From the point spread functions, the corresponding spatial resolutions can be obtained as (see, e.g., [1])

$$\delta_x = \delta_r \approx p\frac{c_0}{2\Delta f}, \tag{20}$$

$$\delta_y = \delta_\varphi \approx p\frac{c_0}{2f_0\Delta\varphi}, \tag{21}$$

$$\delta_z = \delta_\vartheta \approx p\frac{c_0}{2f_0\Delta\vartheta}, \tag{22}$$

where c_0 is the speed of light, f_0 is the center frequency corresponding to k_0 and Δf is the frequency bandwidth. p is an additional factor which may account for different windowing functions ($p \approx 0.89$ for the rectangular window with 3 dB criterion).

For projected 2D imaging in the xy-plane, $h(\Delta\vartheta, z)$ is to be replaced by 1.0 and for imaging in the xz-plane, $h(\Delta\varphi, y)$ is to be replaced by 1.0. Also, the constant $k_0^2/(8\pi^3)$ must be replaced by $k_0/(4\pi^2)$ in both cases.

2.4. Imaging with Shooting and Bouncing Rays Simulations

In an SBR simulation [5, 6], the scattering current distribution $\mathbf{J}^s$ according to (8) is generated via discrete rays hitting the object. For a dense enough grid of rays, the scattering currents without the propagation term of the incident wave are

$$\mathbf{J}(\mathbf{r}') = \sum_{n=1}^{N} \Delta A_n \mathbf{J}_{A,n}\, \mathrm{e}^{-jkl_n}\, \delta\left(x' - x_n, y' - y_n, z' - z_n\right), \tag{23}$$

where N is the number of rays, ΔA_n is the intersection area of the nth ray tube with the scattering object surface and $\mathbf{J}_{A,n}$ is the surface current density magnitude of the nth ray. (x_n, y_n, z_n) is the exit location of the nth ray on the object. In the case of multiple interactions, l_n is the extra path length of the ray due to the multiple interactions causing a linear phase change with k. Analog to the propagation term of the incident wave, this phase term can also be considered in the evaluation of the point spread function in (6). In the small angle/small bandwidth approximation, this extra phase shift will only influence the x-dependence of the point spread function and can be considered as an additional spatial shift according to

$$\mathbf{J}(\mathbf{r}') \approx \sum_{n=1}^{N} \Delta A_n\, \mathbf{J}_{A,n}\, \delta\left(x' - x_n + \frac{l_n}{2}, y' - y_n, z' - z_n\right) \tag{24}$$

equivalent to a shifted virtual exit location of $(x_n - \frac{l_n}{2}, y_n, z_n)$. The resulting convolution in (5) thus becomes

$$\begin{aligned}\hat{\mathbf{J}}(\mathbf{r}) &= \bar{\mathbf{P}}(\mathbf{r}) * \left[\sum_{n=1}^{N} \Delta A_n \, \mathbf{J}_{A,n} \, \delta\left(x - x_n + \frac{l_n}{2}, y - y_n, z - z_n\right)\right] \\ &= \bar{\mathbf{P}}(\mathbf{r}) * \mathbf{J}(\mathbf{r}). \end{aligned} \tag{25}$$

In a numerical simulation, this convolution can be evaluated on a ray-by-ray basis, where the convolutions are directly evaluated employing tabulated point spread functions, which are pre-computed either analytically or numerically. However, a more efficient computation approach is possible by utilizing FFT acceleration. Such a speed-up is very important for practical simulations, if one keeps in mind that many millions of rays are easily necessary for the simulation of a complex target.

The numerical implementation of the imaging approach works with a regular discrete representation of the imaging domain according to

$$\mathbf{r} = (u\Delta x, v\Delta y, w\Delta z) \tag{26}$$

resulting in the discrete representation

$$\hat{\mathbf{J}}_{u,v,w} = \bar{\mathbf{P}}_{u,v,w} * \mathbf{J}_{u,v,w} \tag{27}$$

of the convolution in (25), where the discretization steps can be adapted to the resolutions in the different spatial directions. The discretization steps must, however, be chosen fine enough in order to appropriately represent the point spread functions in (17). This means that the sampling rate must be larger than the corresponding Nyquist frequencies, where in particular the e^{-j2k_0x}-term in in (17) requires at least a sample distance of less than $\lambda_0/4$ in range direction.

2.5. Fast Fourier Transform Accelerated Imaging

Employing the convolution theorem of the discrete Fourier transform, the discrete convolution can by carried out as

$$\hat{\mathbf{J}}_{u,v,w} = \mathrm{FFT}^{-1}\left\{\mathrm{FFT}\left\{\bar{\mathbf{P}}_{u,v,w}\right\} \circ \mathrm{FFT}\left\{\mathbf{J}_{u,v,w}\right\}\right\}, \tag{28}$$

where the discrete Fourier transforms are efficiently computed by FFT and where the $\circ$ denotes an element wise Hadamard product in the discrete Fourier domain. Also, appropriate zero-padding must be considered in order to avoid aliasing errors.

The difficulty with the FFT based implementation is that $\mathbf{J}_{u,v,w}$ must be restricted to its discrete samples, whereas the ray exit points in (25) may have arbitrary locations in the imaging space. Therefore,

the δ-impulses in $\mathbf{J}(\mathbf{r})$ will be represented by interpolations from regular grid samples, what is actually an anterpolation of the ray contributions into the regular grid. An appropriate interpolation or anterpolation formula can be constructed by Lagrange polynomials according to [22]

$$\mathcal{L}_q(\mathbf{r}) = \prod_{l=1}^{3} \prod_{m=1}^{N_p^l} \frac{x^l - x_q^l}{x_m^l - x_q^l} \quad \text{and } q \neq m \tag{29}$$

with $\mathbf{r} = (x^1, x^2, x^3) = (x, y, z)$. Obviously, l indicates the Cartesian vector component, q indicates an interpolation point in the regular grid corresponding to particular (u, v, w)-indices and N_p^l is the number of interpolation points in the particular dimension l. Also, m selects those grid points with the smallest distances to $\mathbf{r}$. An N_p^l-point Lagrange interpolation corresponds to polynomials of order $N_p^l - 1$.

For the interpolation, it must be kept in mind that the δ-impulses in $\mathbf{J}$ have infinite spectral content causing unavoidable aliasing errors. Therefore, the chosen sampling rate must be large enough in order to assure that the aliasing errors are out of the useful low-pass spectrum generated by the spectral multiplication with the low-pass limited FFT $\left\{\bar{\mathbf{P}}_{u,v,w}\right\}$. Employing (17), FFT $\left\{\bar{\mathbf{P}}_{u,v,w}\right\}$ can be calculated analytically but numerically generated point spread function spectra can also be used. Oversampling at least by a factor of 2 is recommended in a numerical implementation.

A reduction of the FFT and of the interpolation from 3D to 2D is straightforward.

By employing the FFT acceleration, the computation time for image generation becomes negligible as compared to the ray-tracing time within the SBR solver.

3. RESULTS

In all simulation examples, the vertical polarization employing the P_{zz}-component of the point spread function has been considered. Higher order terms due to off-diagonal terms in $\bar{\mathbf{P}}$ have not been included.

3.1. Metallic Plate

The first considered example is a metallic plate as illustrated in Fig. 2. The plate is assumed to be much larger than the wavelength λ_0 and it is rotated by 30° with respect to the incident direction. An incident plane wave from x-direction causes homogeneous PO surface currents on the

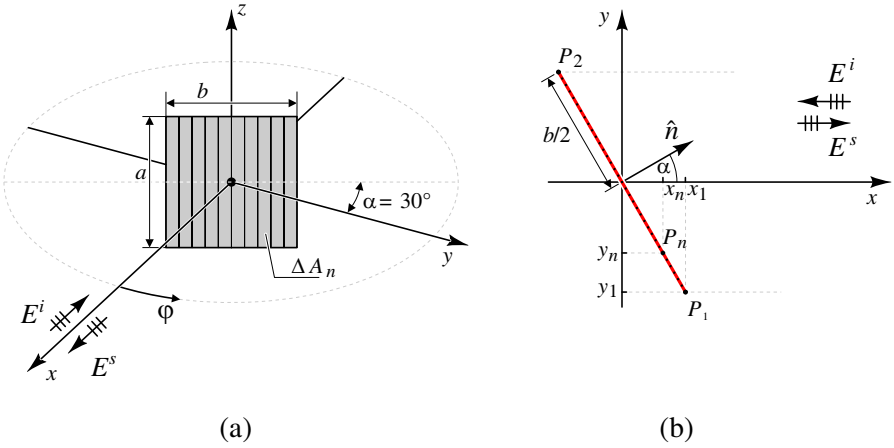

Figure 2. Geometrical configuration of a metallic plate: (a) 3D configuration, (b) projection in xy-plane.

plate (constant magnitude, linear phase with progression dependent on frequency), which are investigated in the following.

For this simple configuration, the Fourier transform of the homogeneous PO currents can be calculated analytically and from this it is easily found that the 2D ISAR image in the xy-plane should consist of two isolated scattering centers at the edges of the plate, i.e.,

$$\hat{J}_z(x,y) = I_0(P_{zz}(x+x_1, y+y_1) - P_{zz}(x-x_1, y-y_1)) \tag{30}$$

where I_0 is a constant dependent on the strength of the incident wave. Fig. 3 shows 2D ISAR images generated with the direct bistatic SBR based imaging approach. The direct convolution according to (25) shows the two scattering centers clearly resolved. The interpolation based fast imaging approaches according to (28) show the scattering centers also clearly, but the suppression of the currents along the plate is limited. The Lagrange interpolation with 5 interpolation points results in better suppression than the linear interpolation.

3.2. Complex Metallic Reference Scattering Object

To study different scattering effects, a *SLICY*-like reference object is used. Similar targets have been investigated by other researchers as well, e.g., [15]. Fig. 4 shows the metallic geometry of the object, which exhibits a series of geometric features causing particular scattering phenomena. Also seen in the figure are the incident or observation directions and a projection of the geometry into the chosen 2D

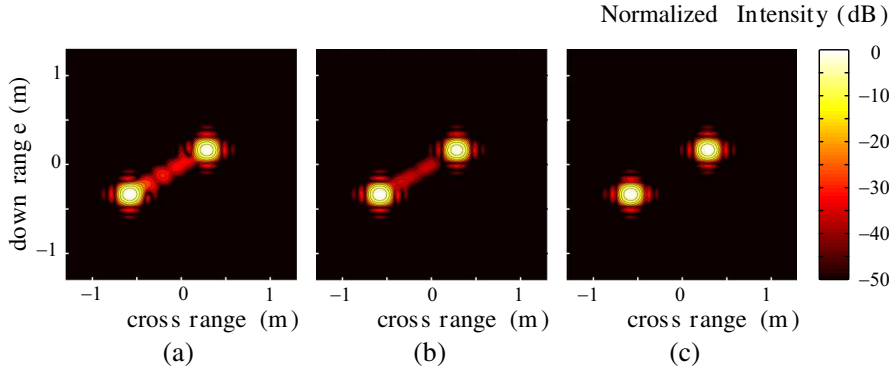

Figure 3. ISAR images of the plate in Fig. 2: (a) Linear interpolation (5 samples per λ_0), (b) Lagrange interpolation (5 interpolation points per dimension, 5 samples per λ_0), (c) direct summation (128×128) without interpolation. The left and right bright spots correspond to P_1 and P_2 in Fig. 2(b), respectively.

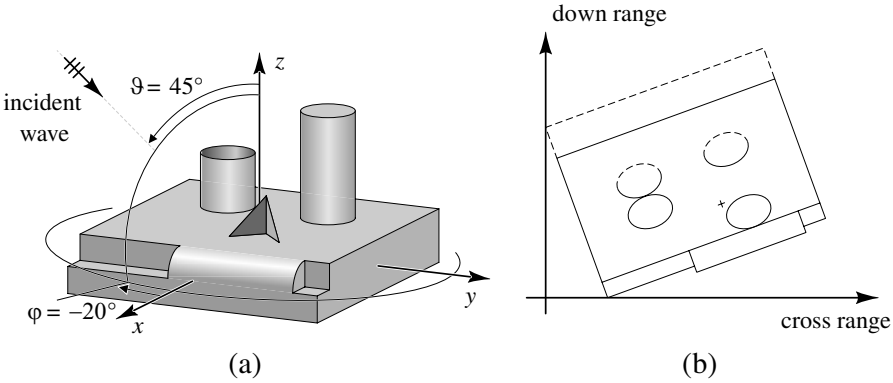

Figure 4. Reference object *SLICY*: (a) Geometry with incidence (observation) direction, where ϑ is kept constant and φ is varying around $\varphi = -20°$ for 2D imaging, (b) projection into 2D imaging plane.

imaging plane. The size of the ground plane of the object is 1 m by 1 m. In Fig. 5, a conventional 2D ISAR image is illustrated where the monostatic scattering data has been computed by an MLFMM accelerated MoM solver [4]. Important scattering contributions in the image are highlighted: ① is due to triple reflections at the corner reflector on the top side of the object, ② indicates a further corner

reflector at the front side of the plate, ③ and ④ are double reflections at the connection of the cylinders with the plate, ⑤ and ⑥ are due to scattering contributions at the front corners of the plate, ⑦ indicates multiple interactions in the open cylinder and ⑧ is due to multiple interactions between plate and cylinder.

ISAR images obtained from SBR simulations are shown in Fig. 6. Compared to the MoM based image, they exhibit some of the scattering phenomena less pronounced, what is expected due to the approximations of the SBR approach. Differences can in particular be found at lower signal levels due to higher order mechanisms or diffraction effects, which have not been captured within the SBR simulations. From Fig. 6 it can, however, be seen that there is, in general, also a good agreement between the images based on the classical Fourier processing of monostatic scattering data and on the bistatic images obtained by the fast direct approach with FFT and interpolation. The main scattering centers, based on double and triple reflections coincide well. Some discrepancies can be observed regarding the peak levels of the triple reflections, which can be attributed to the lack of angular diversity within the fast bistatic simulation approach. In order to be able to compare with the MoM results and to achieve the desired resolution, the relative bandwidth is quite high. For reduced bandwidths in frequency and aspect domains, the presented fast algorithm performs even better. For the chosen simulation parameters and the utilized computer with one core, the computation time for generating the image in Fig. 6(a)) was about 3.2 hours as compared to about 3.5 min required for the image in Fig. 6(b)).

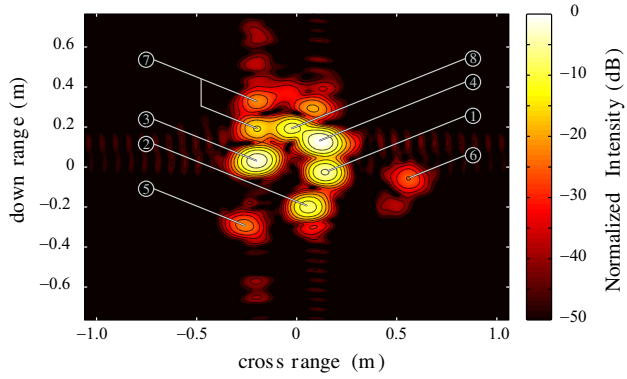

Figure 5. 2D ISAR image of object *SLICY* generated by 32×32 Fourier processing from MoM scattering data, $f_0 = 10\,\mathrm{GHz}$, $\Delta f = 3\,\mathrm{GHz}$, Hamming window.

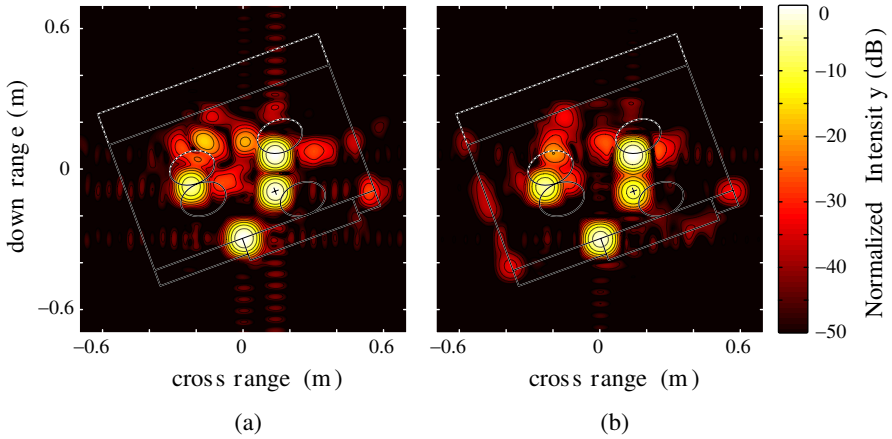

Figure 6. 2D ISAR images of object *SLICY*, $f_0 = 30\,\text{GHz}$, $\Delta f = 3\,\text{GHz}$, Hamming window, $\delta_r \approx \delta_\varphi \approx 0.07\,\text{m}$: (a) Generated by 32×32 Fourier processing of monostatic scattering data from SBR simulations, (b) generated by fast bistatic direct approach with FFT and interpolation.

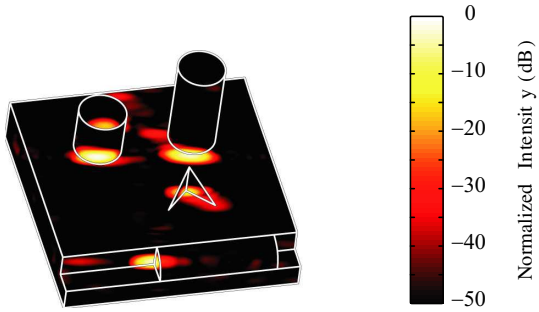

Figure 7. 3D ISAR image projected on the surface of the metallic object, obtained with fast direct algorithm.

Finally, a 3D image of the *SLICY* object is shown in Fig. 7. A fully 3D image has been obtained by the fast bistatic direct approach with FFT acceleration and 5-point Lagrange interpolation and the image has been projected onto the surface of the metallic object. It is clearly seen how the important scattering centers correlate with the geometric features of *SLICY*.

3.3. Automotive Vehicles

Figure 8 shows 2D images of a passenger car and compares the conventional ISAR Fourier processing working with scattering data with the direct image formation. Both images are quite similar, where the directly generated image is even free of the artefacts along the cross range direction in the original ISAR image, which are often observed in coherently processed scattering fields obtained from SBR simulations and which are due to discretization errors [23]. For the chosen simulation parameters and the utilized computer with one core, the computation time for generating the image in Fig. 8(a) was about 161 hours as compared to about 2.6 hours required for the image in Fig. 8(b).

Another 2D ISAR image of a passenger car is depicted in Fig. 9. For this example with a model geometry consisting of more than 600 000 triangular facets, an observation configuration with 30° nose-on angle has been selected. Due to the size of the wheels and wheelhouses multiple reflections play an increased role, which can be clearly seen in form of delayed scattering contributions shifted away from the radar observation point. A direct fast imaging algorithm with FFT acceleration is kind of mandatory for such a complex object. For the

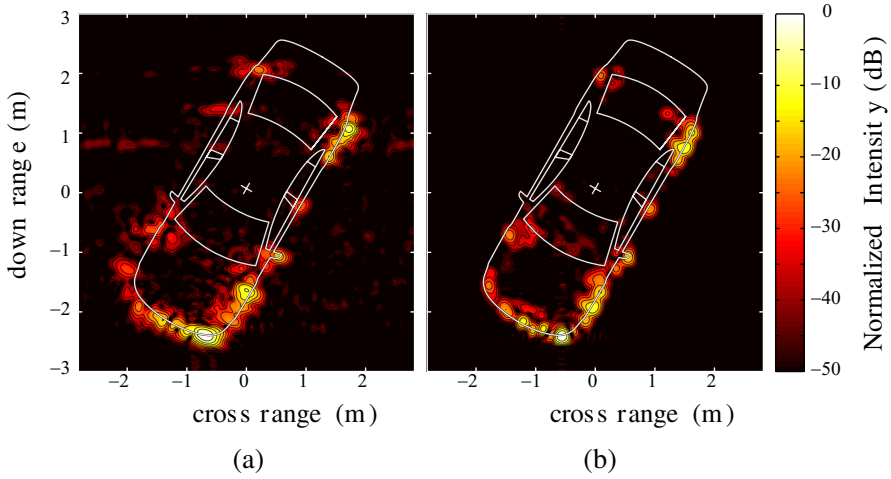

Figure 8. Comparison of 2D monostatic ISAR image simulations of a passenger car at 10 GHz, $\Delta f = 1.5$ GHz, Hamming window, $\delta_r \approx \delta_\varphi \approx 0.13$ m: (a) Image based on monostatic 2D Fourier processing, (b) image obtained by direct bistatic imaging with FFT and interpolation.

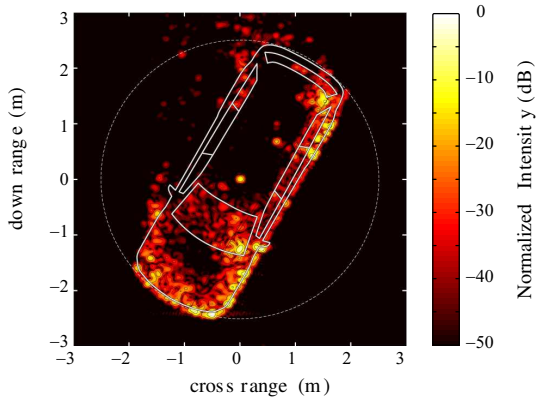

Figure 9. ISAR image of a sports utility vehicle (SUV) obtained by the direct fast algorithm at 24 GHz, $\Delta f = 3$ GHz, Hamming window, $\delta_r \approx \delta_\varphi \approx 0.07$ m. The light scattering center in the rotation center of the car is due to an artificial triple reflector placed for calibration purposes.

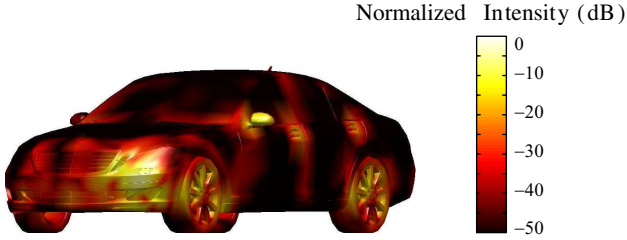

Figure 10. 3D ISAR image projected on the surface of the car body, obtained with fast direct algorithm. The image was obtained with a 3D grid of $256 \times 256 \times 128$ image points in x, y, z-directions, respectively, and $\Delta f = 500$ MHz.

chosen simulation parameters and the utilized computer with one core, the computation time for generating the image in Fig. 9 was about 11 hours.

As a final example, a 3D image of a passenger car is considered. The 3D image was generated by the fast direct imaging approach based on SBR simulations and the scattering centers have been projected onto the surface of the car body. The results are illustrated in Fig. 10 and the dominant scattering centers can clearly be attributed to the corresponding geometrical properties of the car. The computation time for generating this image was about 30 min.

4. CONCLUSION

The direct simulation based image domain formation of Inverse Synthetic Aperture Radar (ISAR) images has been derived in a fully vectorial manner for 3D and 2D image generation. The dyadic point spread functions have been given analytically for the case of small angle/small bandwidth approximation. The approach has been implemented together with a Shooting and Bouncing Rays (SBR) approach for the simulation of metallic scattering objects employing the Physical Optics (PO) approximation, where direct convolution of the individual rays with the pertinent point spread functions can be performed. Tremendous speed-up of the image formation can be achieved by Fast Fourier Transform (FFT) based acceleration of the convolutions including interpolation/anterpolation of the individual ray contributions. Important properties of the various techniques have been discussed and a variety of imaging examples has been considered. It was found that the direct image domain formation of ISAR images is an extremely efficient technique for the generation of realistic bistatic images.

REFERENCES

1. Mensa, D. L., *High Resolution Radar Cross-section Imaging*, Artech House, Norwood, MA, 1991.
2. Bhalla, R. and H. Ling, "ISAR image formation using bistatic data computed from the shooting and bouncing ray technique," *Journal of Electromagnetic Waves and Applications*, Vol. 7, No. 9, 1271–1287, 1993.
3. Peterson, A. F., S. S. Ray, and R. Mittra, *Computational Methods for Electromagnetics*, IEEE Press, Piscataway, 1998.
4. Eibert, T. F., "A diagonalized multilevel fast multipole method with spherical harmonics expansion of the k-space integrals," *IEEE Trans. Antennas Propag.*, Vol. 53, No. 2, 814–817, Feb. 2005.
5. Ling, H., R.-C. Chou, and S.-W. Lee, "Shooting and bouncing rays: Calculating the RCS of an arbitrarily shaped cavity," *IEEE Trans. Antennas Propag.*, Vol. 37, No. 2, 194–205, Feb. 1989.
6. Buddendick, H. and T. F. Eibert, "Acceleration of ray-based radar cross section predictions using monostatic-bistatic equivalence," *IEEE Trans. Antennas Propag.*, Vol. 58, No. 2, 531–539, Feb. 2010.
7. Lee, S. W., H. Ling, and R. Chou, "Ray tube integration in

shooting and bouncing ray method," *Microwave Opt. Tech. Lett.*, Vol. 1, 286–289, Oct. 1988.

8. Bhalla, R. and H. Ling, "Image-domain ray-tube integration formula for the shooting and bouncing ray technique," *Radio Science*, Vol. 30, 1435–1446, Sep./Oct. 1995.
9. Bhalla, R. and H. Ling, "A fast algorithm for signature prediction and image formation using the shooting and bouncing ray technique," *IEEE Trans. Antennas Propag.*, Vol. 43, No. 11, 727–731, Jul. 1995.
10. Bhalla, R. and H. Ling, "Three-dimensional scattering center extraction using the shooting and bouncing ray technique," *IEEE Trans. Antennas Propag.*, Vol. 44, No. 11, 1445–1453, Nov. 1996.
11. Bhalla, R., J. Moore, and H. Ling, "A global scattering center representation of complex targets using the shooting and bouncing ray technique," *IEEE Trans. Antennas Propag.*, Vol. 45, No. 12, 1850–1856, Dec. 1997.
12. Bhalla, R. and H. Ling, "Near-field signature prediction using far-field scattering centers extracted from the shooting and bouncing ray technique," *IEEE Trans. Antennas Propag.*, Vol. 48, No. 2, 337–338, Feb. 2000.
13. Wang, X. B., X. Y. Zhou, T. J. Cui, Y. B. Tao, and H. Lin, "High-resolution inverse synthetic aperture radar imaging based on the shooting and bouncing ray method," *Global Symposium on Millimeter Waves,* Nanjing, China, 2008.
14. He, X. Y., X. B. Wang, Y. Y. Zhou, B. Zhao, and T. J. Cui, "Fast ISAR imag simulation of targets at arbitrarily aspect angles using a novel SBR method," *Progress In Electromagnetics Research B,* Vol. 28, 129–142, 2011.
15. Anglberger, H., R. Speck, T. Kempf, and H. Suess, "Fast ISAR image generation through localization of persistent scattering centers," *Proc. SPIE, Defense & Security*, Orlando, FL, USA, Apr. 2009.
16. Buddendick, H. and T. F. Eibert, "Application of a fast equivalent currents based algorithm for scattering center visualization of vehicles," *IEEE Antennas and Propagation International Symposium,* Toronto, Ca, 2010.
17. Buddendick, H. and T. F. Eibert, "Parallelized physical optics computations for scattering center models in radio channel simulations," *IEEE Vehicular Network Conference,* 2010.
18. Yu, Y., D. Zhang, Z. Yin, and W. Chen, "Broadband electromagnetic scattering echo generation and its ISAR imaging sim-

ulation," *International Conference on Microwave and Millimeter Wave Technology*, Nanjing, China, 2008.

19. Le, C., T. Dogaru, L. Nguyen, and M. A. Ressler, "Ultrawideband (UWB) radar imaging of building interior: Measurements and predictions," *IEEE Transactions on Geoscience and Remote Sensing,* Vol. 47, No. 5, 1409–1419, May 2009.
20. Kong, J. A., *Electromagnetic Wave Theory*, Wiley, New York, 1990.
21. Bleistein, N. and J. K. Cohen, "Nonuniqueness in the inverse source problem in acoustics and electromagnetic," *Journal of Mathematical Physis*, Vol. 18, No. 2, 194–201, Feb. 1977.
22. Abramowitz, M. and I. A. Stegun, *Handbook of Mathematical Functions*, 10th edition, Dover Publications, 1972.
23. Bhalla, R. and H. Ling, "Cross range streaks in ISAR images generated via the shooting and bouncing ray technique: Cause and solutions," *IEEE Antennas Propag. Mag.*, Vol. 39, No. 2, 76–80, Apr. 1997.